Structure, microstructure and microhardness of rapidly solidified Smy(FexNi1-x)4Sb12 (x = 0.45, 0.50, 0.70, 1) thermoelectric compounds

C. Artini, A. Castellero, M. Baricco, M.T. Buscaglia, R. Carlini

Structure, microstructure and microhardness of rapidly solidified $Sm_y(Fe_xNi_{1-x})_4Sb_{12}$ (x = 0.45, 0.50, 0.70, 1) thermoelectric compounds

Solid State Sciences

Volume 79, May 2018, Pages 71–78

DOI: 10.1016/j.solidstatesciences.2018.03.012

Structure, microstructure and microhardness of rapidly solidified $Sm_y(Fe_xNi_{1-x})_4Sb_{12}$ (x = 0.45, 0.50, 0.70, 1) thermoelectric compounds

C. Artini [1,2,], A. Castellero [3], M. Baricco [3], M. T. Buscaglia [2], R. Carlini [1,4]*

[1] Department of Chemistry and Industrial Chemistry, University of Genoa, Via Dodecaneso 31, 16146 Genoa, Italy

[2] CNR-ICMATE, Via De Marini 6, 16149 Genoa, Italy

[3] Department of Chemistry, NIS and INSTM, University of Turin, Via P. Giuria 7, 10125 Turin, Italy

[4] INSTM - Interuniversitary Consortium of Science and Technology of Materials – Genoa Research Unit, Via Dodecaneso 31, 16146 Genoa, Italy

* Corresponding author: artini@chimica.unige.it. Telephone number: +39 010 3536101.

Abstract

Skutterudites are interesting compounds for thermoelectric applications. The main drawback in the synthesis of skutterudites by solidification of the melt is the occurrence of two peritectic reactions requiring long annealing times to form a single phase. Aim of this work is to investigate an alternative route for synthesis, based on rapid solidification by planar flow casting. The effect of cooling rate on phases formation and composition, as well as on structure, microstructure and mechanical properties of the filled $Sm_y(Fe_xNi_{1-x})_4Sb_{12}$ (x = 0.45, 0.50, 0.70, 1) skutterudites was studied. Conversely to slowly cooled ingots, rapidly quenched ribbons show skutterudite as the main phase, suggesting that deep undercooling of the liquid prevents the nucleation of high temperature phases, such as (Fe,Ni)Sb and (Fe,Ni)Sb_2. In as-quenched samples, a slightly out of equilibrium Sm content is revealed, which does not alter the position of the *p*/*n* boundary; nevertheless, it exerts an influence on crystallographic properties, such as the cell parameter and the shape of the Sb_4 rings in the structure. As-quenched ribbons show a fine microstructure of the skutterudite phase (grain size of 2-20 μm), which only moderately coarsens after annealing at 873 K for 4 days. Vickers microhardness values (350-400 HV) of the skutterudite phase in as-quenched ribbons are affected by the presence of softer phases (*i.e.* Sb), which are homogeneously and finely dispersed within the sample. The skutterudite hardens after annealing as a consequence of a moderate grain growth, which limits the matrix effect due to the presence of additional phases.

Keywords

Skutterudites; rapid solidification; crystal chemistry; site occupancy; microstructure; microhardness.

1. Introduction

The current effort in searching materials to be profitably employed in thermoelectric devices is directed toward classes of compounds such as clathrates [1], half-Heusler phases [2], tetrahedrites [3] and paracostibite [4,5]. In addition to these compounds, filled skutterudites play a key role due to the relatively easy tunability of their electronic properties through suitable doping [6,7,8].

Skutterudites MX_3 (M ≡ Co, Rh, Ir and X ≡ P, As, Sb) are known since the first study performed by Oftedal in 1928 [9]. They crystallize in a body-centered cubic cell (Pearson symbol *cI*32, isotypic crystal: $CoAs_3$) belonging to the $Im\bar{3}$ space group, characterized by two atomic positions, namely the 8*c* (¼, ¼, ¼) and the 24*g* (0, *y*, *z*), which are occupied by M and X, respectively. As a consequence of this atomic arrangement, an X_{12} icosahedral cage forms around the 2*a* site located in (0, 0, 0), which can host atoms of proper size, such as alkaline-earths or lanthanides. In the case of complete filling of all the available cavities by a rare earth (RE), the stoichiometry REM_4X_{12} occurs. Filling the cages by the aforementioned atoms results particularly advantageous for efficient thermoelectric materials, since it is generally expected to reduce the phonon mean free path, λ_{ph}, and thus to enhance the figure of merit *ZT* [10]. This prediction is indirectly confirmed in many cases by the high values of the RE displacement parameter [11,12,13,14], which point at the occurrence of a rattling movement of the guest atom within the cavity.

From the electronic point of view, the insertion of a foreign atom into the cell alters the electronic count of the skutterudite. $CoSb_3$, for instance, if treated within the Zintl's concept [15], is expected to be a diamagnetic semiconductor [6], as experimentally confirmed; for this reason it cannot accept the injection of electrons from a foreign atom, which would perturb its electronic stability. On the contrary, if Co is substituted by a lighter transition metal (*e.g.* Fe) or by a Fe/Ni mixture, filling by a cation is needed to compensate the electronic deficiency. In $CeFe_4P_{12}$, for example, Ce^{4+} provides the missing electrons necessary to reproduce the electronic count of a diamagnetic semiconductor [16]. In general, a linear correlation is observed between the amount of

each transition metal M and the content of the filler atom [17]. Nevertheless, since the exact compensation of the electron deficiency by filling is generally not possible, *p*- and *n*-type skutterudites occur, depending on the excess of electrons or holes with respect to the fully compensated diamagnetic semiconductor parent compound. It has been often observed that the amount of filler atom able to enter the structure is dependent on its oxidation state and essentially independent of its chemical identity [7,14], thus implying that even the position of the *p*/*n* crossover is strictly related to the valence state of the filler. In Fe/Ni-based skutterudites, such as in $Sm_y(Fe_{1-x}Ni_x)_4Sb_{12}$ [13,18] and in $DD_y(Fe_{1-x}Ni_x)_4Sb_{12}$ (where DD is didymium, a mixture of Pr and Nd) [19], the *p*/*n* transition is located at *x* ranging between 0.63 and 0.65.

Several methods have been suggested for an effective synthetic procedure of filled skutterudites [20,21] and the most commonly used are derived from the one proposed by Sales *et al.* [22,23]. They consist in a melting process of all the starting elements, followed by a quenching in water or in air, and by a subsequent long annealing in vacuum, which is needed because the two peritectic reactions occurring on solidification are never completed upon cooling. An important issue dealing with the preparation of these compounds in a form suitable for the measurement of transport properties concerns the need for dense bulk samples: this goal is generally achieved by grinding and subsequently densifying the obtained powder by means of techniques such as spark plasma sintering (SPS) [24], hot pressing [12,19,25], cold pressing [17] or open die pressing (ODP) [26,27]. Rapid solidification methods, such as melt spinning [28], are useful to obtain fragile samples, which can be easily crushed and powdered before sintering [26,29]. Moreover, a partial amorphization of the structure can be expected too, which could result in a reduction of the phononic mean free path [30]. In addition, a possible effect of rapid solidification on the appearance or disappearance of small amounts of additional phases, on structural parameters relevant for the electronic properties of the material, as well as on microstructure, cannot be *a priori* excluded.

Aim of this work is to investigate the effects of a processing route based on planar flow casting on the synthesis and properties of skutterudites, since rapid solidification is considered responsible for a significant reduction in the preparation length [31,32]. $Sm_y(Fe_xNi_{1-x})_4Sb_{12}$ (x = 0.45, 0.50, 0.70, 1, y = 0.15, 0.20, 0.45, 0.70) samples underwent rapid solidification followed by an annealing process in vacuum at 873 K. Composition, structural, microstructural and microhardness properties of specimens were investigated, both prior and after the annealing process, and compared to the ones of as sintered samples [13,33], in order to reveal the effect of the rapid solidification and the subsequent thermal treatment on relevant parameters for thermoelectric applications. The results obtained suggest that rapid solidification of $Sm_y(Fe_xNi_{1-x})_4Sb_{12}$ alloys is a promising processing route to obtain single phase precursor materials to be used in the sintering of dense thermoelectric skutterudites.

2. Materials and methods

2.1 Synthesis

Samples belonging to the $Sm_y(Fe_xNi_{1-x})_4Sb_{12}$ system were prepared with nominal x = 0.45, 0.50, 0.70, 1.00 and y = 0.15, 0.20, 0.45, 0.70 by direct reaction of pure elements Fe (Alfa-Aesar, 99.99 wt.%), Ni (Alfa-Aesar, 99.99 wt.%), Sm (NewMet, 99.9 wt.%) and Sb (Mateck, 99.99 wt.%). The Sm amount to be added to each starting mixture was chosen relying on the results reported in [13]; a slight excess of Sb compared to the stoichiometric content was employed to counterbalance possible losses due to its high vapour pressure. Pure elements were mixed as small pieces, put into Ar-filled silica ampoules, subsequently sealed under an Ar flow, and heated up to 1223 K for 3 hours. Quenching in an iced water bath followed. The obtained samples were then annealed in vacuum at 873 K for 4 days (as-sintered samples, AS series [13]).

Rapidly solidified (RS) samples were obtained in the form of fragmented ribbons by a planar flow casting apparatus (Edmund Bühler GmbH). Each alloy obtained after the aforementioned quenching was induction melted under Ar atmosphere in a BN crucible and ejected by an Ar

overpressure (0.2 bar) on a copper wheel rotating at 20 m s^{-1}. The so obtained ribbons (thickness: 20-30 μm) is called RS, and samples are hereafter named Fe40_rs, Fe50_rs and so on, according to the nominal % Fe content with respect to the total (Fe + Ni) amount.

Rapidly solidified samples were subsequently annealed in vacuum at 873 K for 5 days in order to investigate the effect of the thermal process on the structural and microstructural features of the material. The so prepared series is called ANN, and samples are named Fe40_ann, Fe50_ann and so on.

The described samples (RS and ANN series) are compared in terms of structure, microstructure and microhardness to as-sintered samples (AS series), *i.e.* to samples which did not undergo the rapid solidification process; data of the latter are taken from ref. [13].

2.2 SEM-EDS

The overall microstructure, as well as the possible presence of additional phases, the Fe/Ni elemental ratio and the Sm content, were analyzed by scanning electron microscopy (SEM) equipped with energy dispersive x-ray spectroscopy (EDS) (Zeiss EVO 40, with Oxford Instruments Pentafet Link, software package: Oxford-INCA v. 4.07, standard: Co, acceleration voltage: 20 kV, working distance: 12 mm, live time: 40 s). In each ribbon the side cooled in contact with the copper wheel (wheel side) can always be distinguished from the free side (air side). Analyses of unpolished and unetched ribbons were performed both on the wheel and air sides, as well as on the cross sections. Microphotographs were taken by backscattered and secondary electrons, and EDS analyses were carried out on at least eight points or areas for each sample.

2.3 X-ray diffraction

Powders of both rapidly solidified and annealed samples were sieved through a 44 μm sieve, and analyzed by powder x-ray diffraction making use of a Bragg-Brentano powder diffractometer (PANalytical X'pert Pro, Co Kα radiation). Samples were placed on a zero-background Si sample-holder; acquisitions were performed in the angular range 10°-120°, with step 0.02° and time per step 17 s. Diffraction patterns were then refined by the Rietveld method employing the FullProf

software [34]. For all the diffractograms, the background was optimized by linearly interpolating a set of ~ 70 points taken from the experimental pattern, and peak profiles were fitted by the pseudo-Voigt function. In order to obtain accurate values of the lattice parameter, diffraction patterns of each sample were also acquired by using Ge as an internal standard.

2.4 Microhardness

The surface of both as quenched and annealed ribbons of each composition was gently polished prior to be submitted to microhardness measurements, which were carried out by using a Leica VMHT microhardness tester provided with Vickers indenter. A test load of 10 g was applied with a dwell time of 15 seconds, and at least 20 tests were performed on each sample at random positions on the samples surface. Imprints showed diagonals ranging from 6 μm to 10 μm. The corresponding imprints depth (0.9 - 1.5 μm), calculated on the basis of the Vickers indent geometry, does not exceed 1/10 of the ribbon thickness, which is typically set as the empirical limit for avoiding substrate effects [35]. Microhardness data were then divided into distribution frequencies with a width of 30 HV, that enabled to identify the clustering of data around some specific values, as thoroughly discussed in Section 3.4.

3 Results and discussion

3.1 Phase formation and composition

All samples belonging to the RS and the ANN series resulted to be fully crystalline. In all the specimens the filled skutterudite is the main phase, hence its structural model, belonging to the $Im\bar{3}$ space group, was refined. In the last refinement cycles, the structural parameters (the Sb *y* and *z* atomic coordinates, and the Sm and Sb occupancy factors in the 2*a* and 24*g* position, respectively), the scale factor, several peak parameters, and the background points, were simultaneously optimized; atomic isotropic displacement parameters B_{iso} were refined too. Fe and Ni occupancy ratios were fixed to the values obtained from EDS analyses and not allowed to vary, due to the similarity of the x-ray scattering factors of the two atoms, which would reduce the reliability of the

refinement. Additional phases, when present in a significant amount, were included in the refinement too; in particular, the structural models of $FeSb_2$, $NiSb_2$ and Sb were optimized in some samples. The results of Rietveld refinement for sample Fe100_ann is reported as a representative example in Fig. 1. Agreement factors are listed in Table 1, together with the refined compositions of all the samples and the amount of additional phases. It is noteworthy that all the additional phases were revealed by both x-ray diffraction and SEM-EDS, with the only exception of (Fe,Ni)$SmSb_3$, which, due to its tiny amount, was only locally observed by the latter technique.

Table 1 – Refined compositions, refined Sm content of each sample, list of additional phases (as revealed both by x-ray diffraction and by SEM-EDS) and agreement factors of Rietveld refinements (χ^2 and skutterudite R_B).

Sample	*Refined composition*	*Sm content*	*Additional phases*	$\chi^{2\ a)}$	R_B [b)]
Fe40_rs	$Sm_{0.17}(Fe_{0.46}Ni_{0.54})_4Sb_{11.59}$	0.168(2)	$NiSb_2$ [18.6(3) wt.%], Sb (3.7(1) wt.%), (Fe,Ni)$SmSb_3$ [traces, from SEM/EDS].	5.14	3.62
Fe50_rs	$Sm_{0.22}(Fe_{0.49}Ni_{0.51})_4Sb_{11.48}$	0.216(3)	Sb [1.7(1) wt.%]	5.65	5.07
Fe70_rs	$Sm_{0.43}(Fe_{0.70}Ni_{0.30})_4Sb_{12}$	0.432(7)	$FeSb_2$ [0.9(1) wt.%], (Fe,Ni)$SmSb_3$ [traces, from SEM/EDS].	11.6	5.96
Fe100_rs	$Sm_{0.70}Fe_4Sb_{12}$	0.696(2)	$FeSb_2$ [10.2(2) wt.%], Sb [12.7(3) wt.%]	3.83	2.42
Fe40_ann	$Sm_{0.10}(Fe_{0.41}Ni_{0.59})_4Sb_{11.57}$	0.096(8)	$NiSb_2$ [19.3(7) wt.%]	5.57	3.70
Fe50_ann	$Sm_{0.17}(Fe_{0.47}Ni_{0.53})_4Sb_{12}$	0.168(4)	--	7.11	6.54
Fe70_ann	$Sm_{0.43}(Fe_{0.69}Ni_{0.31})_4Sb_{12}$	0.432(7)	$FeSb_2$ [1.8(1) wt.%]	7.91	6.05
Fe100_ann	$Sm_{0.72}Fe_4Sb_{12}$	0.720(3)	$FeSb_2$ [10.9(1) wt.%], Sb [9.3(1) wt.%]	3.11	2.38

a) $\chi^2 = \left(R_{wp}/R_{exp}\right)^2$; $R_{wp} = \left(\frac{\sum w_i\left(Y_{i,obs}-Y_{i,calc}\right)^2}{\sum w_i Y_{i,obs}^2}\right)^{1/2}$; $R_{exp} = \left(\frac{N-P}{\sum w_i Y_{i,obs}^2}\right)^{1/2}$, where w_i is the statistical weight of the *i*-th measure, $Y_{i,obs}$ and $Y_{i,calc}$ are the observed and the calculated intensity of the *i*-th 2θ value respectively, N and P are the number of experimental points and of refined parameters, respectively.

b) $R_B = \frac{\sum |Y_{k,obs}-Y_{k,calc}|}{\sum_k |Y_{k,obs}|}$, where $Y_{k,obs}$ and $Y_{k,calc}$ are the observed and the calculated intensity of the *k*-th Bragg peak, respectively.

In Fig. 2a the presence of (Fe,Ni)$SmSb_3$ on the edge of sample Fe70_ann is highlighted. Moreover, by inspection of the microphotograph taken on the wheel side of sample Fe40_rs (Fig. 2b), it is possible to notice that the crystalline habit of (Fe,Ni)$SmSb_3$ phase agrees with the orthorhombic shape of the cell, which belongs to the $Pbcm$ space group.

For each composition, no significant differences in the Fe and Ni content were observed between RS and ANN samples. Regarding the content of elemental Sb, on the contrary, a remarkable reduction seems to be caused by the annealing process (see Table 1), which could promote the partial evaporation of Sb, because of the high vapor pressure of this element (10^{-3} mm Hg at 873 K [36]). Even the incorporation of Sb into the skutterudite as a consequence of the thermal process cannot be excluded, but due to the much larger amount of the latter with respect to free Sb, it cannot be appreciated by x-ray diffraction. It is worth noting that a previous study of this group showed that thermal processes lead to an imbalance of the Sb amount between the center and the border of the skutterudite grains, with a higher content in the region of the boundaries, as evidenced by EDS analyses [33].

Moreover, a general trend can be also recognized in the Sm content (see Table 1), which in all the RS samples (except in Fe100) is slightly higher than in ANN specimens, and significantly higher than in samples belonging to the AS series [13]; this issue will be discussed later in more detail.

As aforementioned, the most abundant additional phases found in the samples studied are $FeSb_2$ (in Fe-rich compositions), $NiSb_2$ (in Ni-rich compositions) and Sb; $FeSb_2$ and $NiSb_2$ can be easily distinguished by x-ray diffraction, since they belong to different space groups ($Pnn2$ and $Pnnm$, respectively) with respect to the skutterudite. At this stage, it is worth to underline that, with respect to as-sintered samples [13], the as-quenched ones, in particular samples Fe50_rs and Fe70_rs, are characterized by a smaller amount of additional phases. The explanation of this evidence has to be pursued in the features of the ternary Fe-Ni-Sb phase diagram [37]. According to the isopleth at 75 at.% Sb, the (Fe,Ni)Sb_3 skutterudite phase is stable below 915 K when the Fe

content is around 12.5 at.%, whereas the end members $FeSb_3$ and $NiSb_3$ are not stable. The stability field of the $(Fe,Ni)Sb_3$ skutterudite phase is considerably extended ($11.25 \leq$ Fe at.% ≤ 25.00) by the addition of Sm [13].

The presence of the two peritectic reactions [37]

$$1018\ K \qquad L + (Fe,Ni)Sb \rightarrow (Fe,Ni)Sb_2 \qquad (1)$$

$$915\ K \qquad L + (Fe,Ni)Sb + (Fe,Ni)Sb_2 \rightarrow (Fe,Ni)Sb_3 \qquad (2)$$

requires a long annealing before the formation of the skutterudite phase is completed [13]. As shown in Table 1, as quenched samples (RS series) contain relevant amounts of the skutterudite phase (reaching 99 wt.% for sample Fe70_rs), suggesting that rapid solidification favours the direct formation of the desired phase. This result can be explained in two ways. On one hand, the formation of the phases stable at high temperature, *i.e.* (Fe,Ni)Sb and $(Fe,Ni)Sb_2$, can be kinetically inhibited through deep undercooling of the liquid, which directly solidifies into the skutterudite $(Fe,Ni)Sb_3$. On the other hand, undercooling of the liquid favours nucleation with respect to grain growth, leading to a refined microstructure of the phases stable at high temperature, which rapidly complete the peritectic reactions due to the limited diffusion path. A combination of the two mechanisms is indeed possible. The presence of a higher amount of additional phases in samples Fe40_rs and Fe100_rs is likely due to the occurrence of different solidification paths owing to the deviation from the cited stoichiometry (12.5% at. Fe, 12.5% at. Ni), as observable in the aforementioned isopleth [37].

No significant differences can be observed by comparing the amounts of the additional phases before and after the annealing process. Therefore, the thermal treatment performed at 873 K subsequently to rapid solidification is not sufficient to promote the solid state reaction between $(Fe,Ni)Sb_2$ and Sb to form $(Fe,Ni)Sb_3$ in Fe40_rs and Fe100_rs.

3.2 Structural properties

The obtained cell parameters are reported in Fig. 3 as a function of the Fe content for as-quenched and annealed samples; in order to make a comparison, data from AS samples (taken from [13]) are shown too. It is noteworthy that all the cell parameters shown were calculated by using Ge as an internal standard, so that they have to be considered very accurate; uncertainties were obtained from the least squares method and range between $1 \cdot 10^{-4}$ and $3 \cdot 10^{-4}$ Å.

As widely discussed in [13,18], the most relevant evidence observable in the AS series consists in the presence of a sharp discontinuity in the cell parameters trend at the *p*/*n* crossover, due to the steeper increase of *a* as a function of the Fe content in the *p* than in the *n* region. The origin of the slope change is still unclear, but it has been suggested to be related to a possible low- to high-spin transition of Fe^{2+}, occurring at the *p*/*n* crossover with increasing the Fe content [13]. Samples studied in the present work seem to follow the described trend, with the Fe-rich compositions characterized by a remarkably larger cell parameter than the Ni-rich ones. If RS and AS samples are compared, the most significant difference concerns the higher value of the cell parameter of the former; the thermal treatment following the rapid solidification does not substantially change the described scenario, since in ANN samples the deviation from as sintered samples is only partly recovered. It is plausible that the larger cell parameter of RS samples in comparison to the AS ones is related to the aforementioned higher Sm content shown by samples with similar Fe-content. In fact, in spite of the oversized volume of the cavity hosting Sm atoms, which guarantees the rattling movement of the guest atom around its equilibrium position, it has been experimentally found that the cage size is sensitive to its atomic content (since it increases with increasing the Sm amount), and hence that the Sm content influences the value of the lattice parameter too [13].

The higher Sm content in almost all the RS samples with respect to the AS ones can potentially influence the electronic properties of the material. It is in fact well known that the electronic count deriving from the presence of the filler atom compared to the one of the parent compound is the critical parameter which determines the *n* or *p* nature of the skutterudite. Moreover, the concentration of the guest atom corresponding to the *p*/*n* crossover is generally independent of the

chemical identity of the filler, but it is dependent on oxidation state [7] In addition to these factors, the results of this study (see Table 1) suggest that even the synthetic route can contribute to the filler amount. In Fig. 4 the Sm amount is reported as a function of the Fe amount for all the three series of samples; the black solid line represents the Sm amount theoretically needed to reproduce the electronic count of the parent compound $CoSb_3$ [7,13], *i.e.* of a compensated skutterudite, while the other ones are the regression lines fitting the experimental points. The crossing point of the black line with each of the other ones represents the position of the *p*/*n* crossover for the given series. The small difference in the Sm amount between as sintered and as quenched samples affects the slopes of the regression lines, since they span from 1.20 (AS series) to 0.96 (AS series); nevertheless, the position of the boundary is substantially the same for all the series. Moreover, the very small difference between Sm contents referred to RS and ANN samples suggests that the performed thermal treatment is not able to restore the equilibrium concentration of Sm, thus further confirming the already described effect of the annealing process on the lattice parameters.

Another peculiarity related to the structural features of filled skutterudites concerns the shape of the Sb_4 rings, which is strictly dependent on the Sb *y* and *z* fractional coordinates in the 24*g* atomic site [6]. As a general remark, in these compounds an increase in the filler atom content induces a corresponding increase in the *y* and *z* coordinates; in Sb-based skutterudites, in particular, the $(y + z)$ sum approaches and in some cases exceeds the Oftedal's relation

$$y + z = 0.5 \quad (1)$$

depending on the identity of the transition element [9,11,20].

The value 0.5 corresponds to an ideally square Sb_4 ring, as pointed out by Jeitschko and Braun [38], who thoroughly studied the geometric relations within filled skutterudites. (Fe,Co)-based antimonides, for instance, present square Sb_4 rings when the cage is completely filled [11]; at variance, in the case of (Fe,Ni)-containing antimonides, the Oftedal's relation is never reached, since even the highest guest atom concentration accepted by the matrix is not sufficient to completely fill all the available cavities [13]. In Fig. 5 the $(y + z)$ sum is reported as a function of

the Fe amount for AS and RS samples: it is noteworthy that the latter present values higher than the former at each composition, particularly in Ni-richer samples; moreover, the increase of the $(y + z)$ values is less steep for the as quenched samples. The described evidences are in good agreement with the larger Sm content in the RS specimens with respect to the AS ones.

Values of both the longer and the shorter Sb-Sb distances within the Sb_4 rings, calculated by using the refined *y* and *z* fractional coordinates of site 24*g*, are reported as a function of the Sm content in Fig. 6. It can be observed that the tendency to reach a common value with increasing Sm, *i.e.* to assume the square shape, is retained even in as quenched samples; nevertheless, it is less marked than in the AS ones, as a direct consequence of the observed less steep increase of the $(y + z)$ sum in rapidly solidified specimens. The described behaviour is particularly evident in the trend of the longer Sb-Sb distance, which shows substantially constant values with changing the Fe content.

3.3 Microstructure

The thickness of the rapidly solidified ribbons, evaluated by SEM images of the cross section, ranges between 20 μm and 30 μm, as shown in Fig. 2 in the case of sample Fe70_ann. The inspection of this part of the ribbon enables also to recognize the side of the edge located close to the wheel side, thanks to the presence of smaller skutterudite grains aligned along the corresponding border.

The wheel side of ribbons presents stripes clearly observable by SEM (a detail is shown for example in Fig. 7), which do not disappear even after the subsequent thermal treatment. In addition to the edge, the formation of additional phases is observed also on this side of the ribbon, as evidenced for instance in Fig. 2b by the presence of $(Fe,Ni)SmSb_3$ on the surface of the wheel side of sample Fe40_rs.

On the air side, on the contrary, it can be observed the formation almost of the sole skutterudite with grains of different sizes, ranging in particular between ~2 μm and ~20 μm, as shown for example in Figs. 8(a) and 8(b).

3.4 Microhardness

Indentations were performed at random positions on the unetched samples surfaces in order to obtain a rough estimation of the statistical distribution of phases. By analyzing the calculated distribution frequencies, it can be noticed that the obtained results cluster around three values, namely 400-450 HV, 350 HV and 150-200 HV, with slight differences between as-quenched and annealed specimens which will be hereinafter discussed. In Fig. 9 the microhardness distribution frequencies (%) found for the RS and ANN series of sample Fe_100 are reported as an example. The distribution with the highest frequency is observed for the values around 400-450 HV, and relying on this evidence, as well as on the comparison with the microhardness values reported in the literature for Fe/Ni filled skutterudites [21], it has been attributed to the main phase. The distribution frequency clustering around 150-200 HV has been ascribed to the presence of Sb, in accordance with the conclusions drawn in [33]; the described attribution is in good agreement with the amount of Sb in Fe100_ann revealed by x-ray diffraction (see Table 1). Finally, the distribution frequency centred at 350 HV (which is overlapped to the one centred around 350-400 HV in the case of sample Fe100_rs) can be attributed to the presence of $FeSb_2$.

According to Rogl *et al.* [21], Vickers hardness values of some of the aforementioned skutterudites are revealed around 550 HV ($HV_{0.1}$ = 540 ± 18 for $Ba_{0.09}Sr_{0.02}DD_{0.22}Yb_{0.02}Fe_{2.4}Ni_{1.6}Sb_{12}$ and $HV_{0.1}$ = 560 ± 20 for $Ba_{0.15}Yb_{0.05}DD_{0.28}Fe_3NiSb_{12}$); a previous work of this research group, in accordance with the cited paper, attributes to the $Sm_y(Fe_xNi_{1-x})_4Sb_{12}$ system microhardness values ranging between 450 and 520 HV [33]. Average microhardness values of the skutterudite phase in all the alloys studied in this work, were calculated from the data clustered around 400-450 HV, and are reported in Fig. 10 for as quenched ribbons,

annealed ribbons and as-sintered samples [33]. It can be observed that the values for the rapidly solidified (350-400 HV) and annealed (380-430 HV) samples are significantly lower than those of the AS series (450-520 HV).

The observed underestimation of microhardness values for the skutterudite phase contradicts the general expectation for higher hardness in rapidly solidified samples, typically due to grain refinement. This unexpected result can be most probably correlated to the specific peculiarities of the microstructure of RS samples, as well as to the way microhardness measurements were performed. As aforementioned, in fact, indentations were done at random positions on unetched samples; thus, it cannot be excluded that some of them involve more than one phase, and this possibility is made even more probable by the very fine microstructure of as quenched samples.
Thus, microhardness measurements of the skutterudite phase are affected by the fine dispersion of softer $(Fe,Ni)Sb_2$ and Sb within $Sm_y(Fe_xNi_{1-x})_4Sb_{12}$, which leads to values lower than expected. It is noteworthy that the hardness values obtained for Sb within the present samples are much higher than the ones commonly reported for pure Sb (50-70 HV) [39]. Sb results to be significantly harder than pure Sb because it is finely dispersed in the matrix consisting of the skutterudite and $(Fe,Ni)Sb_2$.

After annealing, distribution frequencies of all the phases (ANN series) become narrower than in the as quenched case (RS series), as a consequence of the grain growth due to the thermal process, which makes microhardness values more representative of each phase. In fact, larger values for the skutterudite and lower values for Sb are observed with respect to as quenched samples, in accordance with the expected trend. In more detail, annealed samples show microhardness values of the skutterudite which are intermediate between the ones of the RS and AS series, as observable in Fig. 10.

4 Conclusions

The structural, microstructural and microhardness study performed on as-quenched rapidly solidified and subsequently annealed samples belonging to the $Sm_y(Fe_xNi_{1-x})_4Sb_{12}$ system allows to draw the following main conclusions:

- rapid solidification promotes the formation of the skutterudite as the main phase (78-99 wt. %) with small amounts of additional phases, thus significantly improving the results obtained in as-sintered samples. This evidence suggests that deep undercooling of the melt inhibits the nucleation of high temperature phases, such as (Fe,Ni)Sb and $(Fe,Ni)Sb_2$, bypassing the two peritectic reactions that slow down the formation of the skutterudite phase. Thus, rapid solidification reveals to be a promising technique for processing single phase skutterudites avoiding long annealing treatments.
- the rapid cooling process exerts an influence on the skutterudite Sm content, which results slightly higher than in equilibrium conditions. As a consequence, the lattice parameter is affected, as well as the Sb-Sb interatomic distances and the shape of the Sb_4 rings. The composition corresponding to the skutterudite *p*/*n* crossover, on the contrary, is not altered. The excess Sm content is only partly recovered by the annealing treatment;
- as-quenched ribbons show a refined microstructure where skutterudite grain size ranges from 2 μm to 20 μm, and additional phases, when present, are uniformly and finely dispersed;
- the rapid cooling process does not promote neither the amorphization of the skutterudite, nor its hardening. Microhardness of the skutterudite phase in as-quenched ribbons is affected by the presence of soft additional phases (*e.g.* Sb); this effect becomes less evident in the annealed ribbons as a consequence of the grain growth promoted by the thermal treatment.

Conflicts of interest

No conflicts of interest exist.

Acknowledgements

Authors are indebted to Dr. G. Fiore (University of Turin) for the rapid solidification process and Dr. P. Piccardo (University of Genoa) for the microhardness measurements. A. Castellero and M. Baricco thank Fondazione CRT for financial support (Grant. N. 2015/1530).

Figure captions

Figure 1 – Rietveld refinement plot of sample Fe100_ann. The dotted (red) and the continuous (black) lines are the experimental and the calculated diffractogram, respectively. The lower (blue) line is the difference curve. The vertical bars indicate the calculated positions of Bragg peaks: blue bars: skutterudite; red bars: Sb; green bars: $FeSb_2$.

Figure 2 – a) Microphotograph taken by secondary electrons on the edge of sample Fe70_ann; it is possible to observe the presence of small amounts of the additional phase (Fe,Ni)$SmSb_3$; the presence of skutterudite grains with different sizes allows to distinguish the wheel side from the air side. b): SEM microphotograph taken by backscattered electrons of sample Fe40_rs. The presence of small amounts of (Fe,Ni)$SmSb_3$ within the skutterudite-based matrix is highlighted; it is also possible to observe the crystalline habit of the phase.

Figure 3 – Trend of the cell parameters of as sintered (from [13]), as quenched and annealed samples as a function of the Fe amount. Error bars are hidden by data markers. The red vertical dashed line indicates the position of the *p*/*n* crossover.

Figure 4 – Trend of the Sm content (*y*) as a function of the Fe content (*x*) for as sintered (data taken from [13]), as quenched and annealed samples; error bars are hidden by data markers. The colored solid lines are the regression lines fitting experimental points, while the black line indicates the theoretical Sm amount needed to reproduce the electronic count of a compensated skutterudite. Vertical dashed lines highlight the position of the *p*/*n* crossover for each series of samples.

Figure 5 – Refined sum of the *y* and *z* fractional coordinates of Sb for as sintered [13] and as quenched samples. The green and the pink line are guides for the eye related to data of as sintered and as quenched samples, respectively.

Figure 6 – Trend of the Sb-Sb interatomic distances within the Sb_4 ring for as sintered, as quenched and annealed samples as a function of the Sm content. Solid and dashed lines are the regression lines fitting experimental data.

Figure 7 – Microphotograph taken by backscattered electrons on the surface of sample Fe40_ann cooled in contact with the copper wheel.

Figure 8 – Microphotograph taken a) by secondary electrons on the air side surface of sample Fe100_ann and b) by backscattered electrons on the sir side surface of sample Fe50_rs.

Figure 9 – Distribution frequencies (%) of the microhardness values found for samples Fe100_rs and Fe100_ann.

Figure 10 – Average values of the skutterudite microhardness for samples belonging to the AS, RS and ANN series. Errors bars correspond to the standard deviation; dashed lines are a guide for the eye.

References

[1] J. Fu, X. Su, Y. Yan, W. Liu, Z. Zhang, X. She, C. Uher, X. Tang, Thermoelectric properties of Cu/Ag doped type-III $Ba_{24}Ge_{100}$ clathrates, J. Solid State Chem. 253 (2017) 414-420.

[2] A. Tavassoli, F. Failamani, A. Grytsiv, G. Rogl, P. Heinrich, H. Müller, E. Bauer, M. Zehetbauer, P. Rogl, On the Half-Heusler compounds $Nb_{1-x}\{Ti,Zr,Hf\}_xFeSb$: Phase relations, thermoelectric properties at low and high temperature, and mechanical properties, Acta Mater. 135 (2017) 263-276.

[3] R. Chetty, A. Bali, M.H. Naik, G. Rogl, P. Rogl, M. Jain, S. Suwas, R. C. Mallik, Thermoelectric properties of Co substituted synthetic tetrahedrite, Acta Mater. 100 (2015) 266-274.

[4] R. Carlini, C. Artini, G. Borzone, R. Masini, G. Zanicchi, G. A. Costa, Synthesis and characterization of the compound CoSbS, J. Therm. Anal. Calorim. 103 (2011) 23-27.

[5] R. Chmielowski, S. Bhattacharya, W. Xie, S. Jacob, K. Moriya, A. Weidenkaff, G. K. H. Madsen and G. Dennler, High thermoelectric performance of tellurium doped paracostibite, J. Mater. Chem. C 4 (2016) 3094-3100.

[6] B. C. Sales, Filled skutterudites, in: K. A. Gschneidner Jr., J.-C. G. Bünzli and V. K. Pecharsky (Eds.), Handbook on the Physics and Chemistry of Rare Earths, North Holland, 2003, 33, pp. 1-34.

[7] C. Uher, Skutterudite-based thermoelectric, in D. M. Rowe (Ed.), Thermoelectrics Handbook – Macro to Nano, Taylor and Francis, 2006, ch. 34, pp. 1-17.

[8] J. R. Sootsman, D. Y. Chung, M. G. Kanatzidis, New and old concepts in thermoelectric materials, Angew. Chem. Int. Ed. 48 (2009) 8616-8639.

[9] I. Oftedal, Die Kristallstruktur von Skutterudit und Speiskobalt-Chloanthit, Z. Kristallogr. A 66 (1928) 517-546.

[10] C. Uher, In search of efficient n-type skutterudite thermoelectrics, Thermoelectrics, Proceedings of the XXI International Conference on Thermoelectrics (2002) 35-41.

[11] B. C. Chakoumakos, B. C. Sales, Skutterudites: Their structural response to filling, J. Alloys Compd. 407 (2006) 87-93.

[12] A. Kaltzoglou, P. Vaqueiro, K. S. Knight, A. V. Powell, Synthesis, characterization and physical properties of the skutterudites $Yb_xFe_2Ni_2Sb_{12}$ ($0 \leq x \leq 0.4$), J. Solid State Chem. 193 (2012) 36-41.

[13] C. Artini, G. Zanicchi, G.A. Costa, M. M. Carnasciali, C. Fanciulli, R. Carlini, Correlations between structural and electronic properties in the filled skutterudite $Sm_y(Fe_xNi_{1-x})_4Sb_{12}$, Inorg. Chem. 55 (2016) 2574-2583.

[14] D. Bérardan, E. Alleno, C. Godart, O. Rouleau, J. Rodriguez-Carvajal, Preparation and chemical properties of the skutterudites $(Ce\text{-}Yb)_yFe_{4-x}(Co/Ni)_xSb_{12}$, Mater. Res. Bull. 40 (2005) 537-551.

[15] E.S. Toberer, A.F. May, G.J. Snyder, Zintl chemistry for designing high efficiency thermoelectric materials, Chem. Mater. 22 (2010) 624-634.

[16] S. V. Dordevic, N. R. Dilley, E. D. Bauer, D. N. Basov, M. B. Maple, L. Degiorgi, Optical properties of MFe_4P_{12} filled skutterudites, Phys. Rev. B 60 (1999) 11321-11328.

[17] L. Chapon, D. Ravot, J. C. Tedenac, Nickel-substituted skutterudites: synthesis, structural and electric properties, J. Alloys Compd. 282 (1999) 58-63.

[18] C. Artini, C. Fanciulli, G. Zanicchi, G. A. Costa, R. Carlini, Thermal expansion and high temperature structural features of the filled skutterudite $Sm_{\beta}(Fe_{\alpha}Ni_{1-\alpha})_4Sb_{12}$, Intermetallics 87 (2017) 31-37.

[19] G. Rogl, A. Grytsiv, E. Bauer, P. Rogl, M. Zehetbauer, Thermoelectric properties of novel skutterudites with didymium: $DD_y(Fe_{1-x}Co_x)_4Sb_{12}$ and $DD_y(Fe_{1-x}Ni_x)_4Sb_{12}$, Intermetallics 18 (2010) 57-64.

[20] D. J. Braun, W. Jeitschko, Preparation and structural investigations of antimonides with the $LaFe_4P_{12}$ structure, J. Less Common Met. 72 (1980)147-156.

[21] G. Rogl, A. Grytsiv, E. Royanian, P. Heinrich, E. Bauer, P. Rogl, M. Zehetbauer, S. Puchegger, M. Reinecker, W. Schranz, New p- and n-type skutterudites with ZT>1 and nearly identical thermal expansion and mechanical properties, Acta Mater. 61 (2013) 4066-4079.

[22] B. C. Sales, D. Mandrus, R. K. Williams, Filled skutterudite antimonides: A new class of thermoelectric materials, Science 272 (1996) 1325-1328.

[23] B. C. Sales, D. Mandrus, B. C. Chakoumakos, V. Keppens, J. R. Thompson, Filled skutterudite antimonides: Electron crystals and phonon glasses, Phys. Rev. B 56 (1997) 15081-15089.

[24] A. U. Khan, K. Kobayashi, D.-M. Tang, Y. Yamauchi, K. Hasegawa, M. Mitome, Y. Xue, B. Jian, K. Tsuchiya, D. Golberg, Y. Bando, T. Mori, Nano-micro-porous skutterudites with 100% enhancement in ZT for high performance thermoelectricity, Nano Energy 31 (2017) 152-159.

[25] B. Bourgouin, D. Bérardan, E. Alleno, C. Godart, O. Rouleau, E. Leroy, Preparation and thermopower of new mischmetal-based partially filled skutterudites $Mm_yFe_{4-x}(Co/Ni)_xSb_{12}$, J. Alloys Compd. 399 (2005) 47-51.

[26] A. Castellero, C. Fanciulli, R. Carlini, G. Fiore, P. Mele, F. Passaretti, M. Baricco, Effect of processing routes on the synthesis and properties of Zn_4Sb_3 thermoelectric alloy, J. Alloys Compd. 653 (2015) 54-60.

[27] S. Battiston, C. Fanciulli, S. Fiameni, A. Famengo, S. Fasolin, M. Fabrizio, One step synthesis and sintering of Ni and Zn substituted tetrahedrite as thermoelectric material, J. Alloys Compd. 702 (2017) 75-83.

[28] H. Kitagawa, M. Hasaka, T. Morimura, H. Nakashima, S. Kondo, Skutterudite structure and thermoelectric property in $Ce_fFe_{8-x}Co_xSb_{24}$, Mater. Res. Bull. 35 (2000) 185-192.

[29] A. Castellero, G. Fiore, E. Evenstein, M. Baricco, Y. Amouyal, Effects of Rapid Solidification on Phase Formation and Microstructure Evolution of $AgSbTe_2$-Based Thermoelectric Compounds, J. Nanosci. Nanotechnol. 17 (2017) 1650-1656.

[30] T. Zhu, Y. Liu, C. Fu, J.P. Heremans, J.G. Snyder, X. Zhao, Compromise and synergy in high-efficiency thermoelectric materials, Adv. Mater. 29 (2017) 1605884.

[31] N. Shaheen, X. Shen, M. S. Javed, L. Guo, A. Zhang, X. Lu, G. Wang, X. Zhou, Super-fast preparation of Nd-filled p-type skutterudites compounds with enhanced thermoelectric properties, Cer. Int. 43 (2017) 7443-7447.

[32] G. Tan, W. Liu, S. Wang, Y. Yan, H. Li, X. Tang, C. Uher, Rapid preparation of $CeFe_4Sb_{12}$ skutterudite by melt spinning: rich nanostructures and high thermoelectric performance, J. Mater. Chem. A 1 (2013) 12657-12668.

[33] C. Artini, R. Carlini, Influence of composition and thermal treatments on microhardness of the filled skutterudite $Sm_y(Fe_xNi_{1-x})_4Sb_{12}$, J. Nanosci. Nanotechnol. 17 (2017) 1634-1639.

[34] J. Rodriguez-Carvajal, Recent advances in magnetic structure determination by neutron powder diffraction, Physica B 192 (1993) 55-69.

[35] "Standard Test for Microhardness of Materials", ASTM Standard Test Method E-384, Annual Book of Standards 3.01, American Society for Testing and Materials, Philadelphia, PA 1989, p. 469.

[36] R. C. Weast, Handbook of Chemistry and Physics, CRC Press, Cleveland, 1976.

[37] K.W. Richter, H. Ipser, An experimental investigation of the Fe-Ni-Sb ternary phase diagram, J. Phase Equilibria 18 (1997) 235-244.

[38] W. Jeitschko, D. J. Braun, $LaFe_4P_{12}$ with filled $CoAs_3$-type structure and isotypic lanthanoid-transition metal polyphosphides, Acta Cryst. B 33 (1977) 3401-3406.

[39] B. Lafuente, R. T. Downs, H. Yang and N. Stone, in: T. Armbruster and R. M. Danisi (Eds.), Highlights in Mineralogical Crystallography, W. De Gruyter, 2015, p. 1.

Figure 1

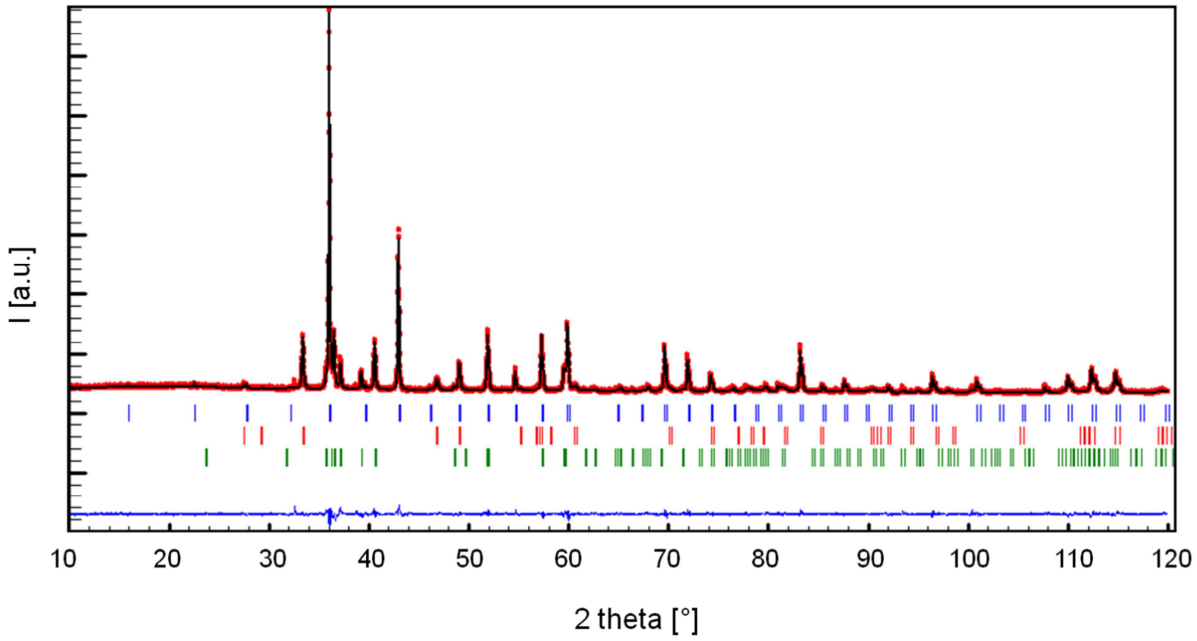

Figure 2

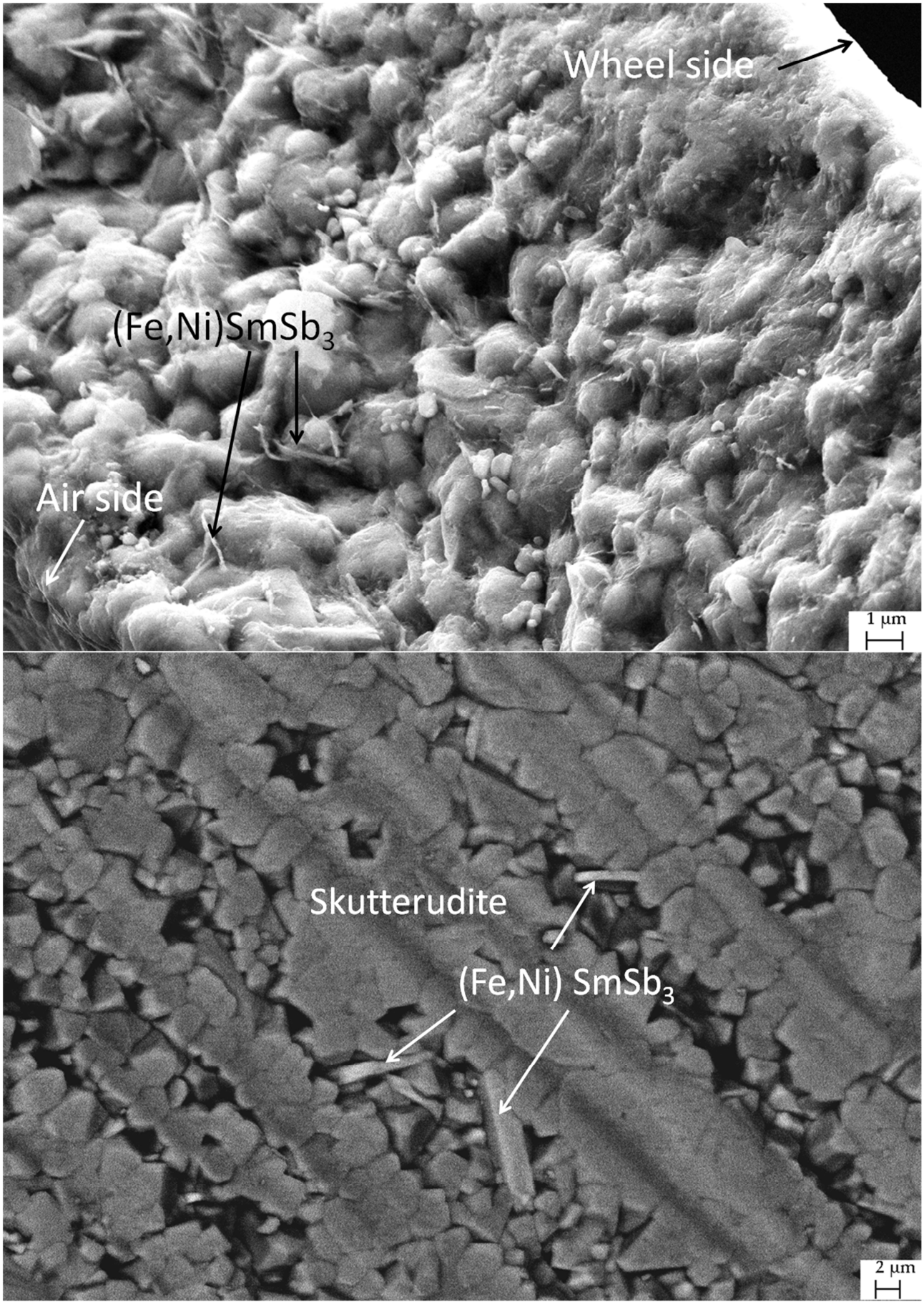
Wheel side
(Fe,Ni)SmSb3
Air side
1 μm
Skutterudite
(Fe,Ni) SmSb3
2 μm

Figure 3

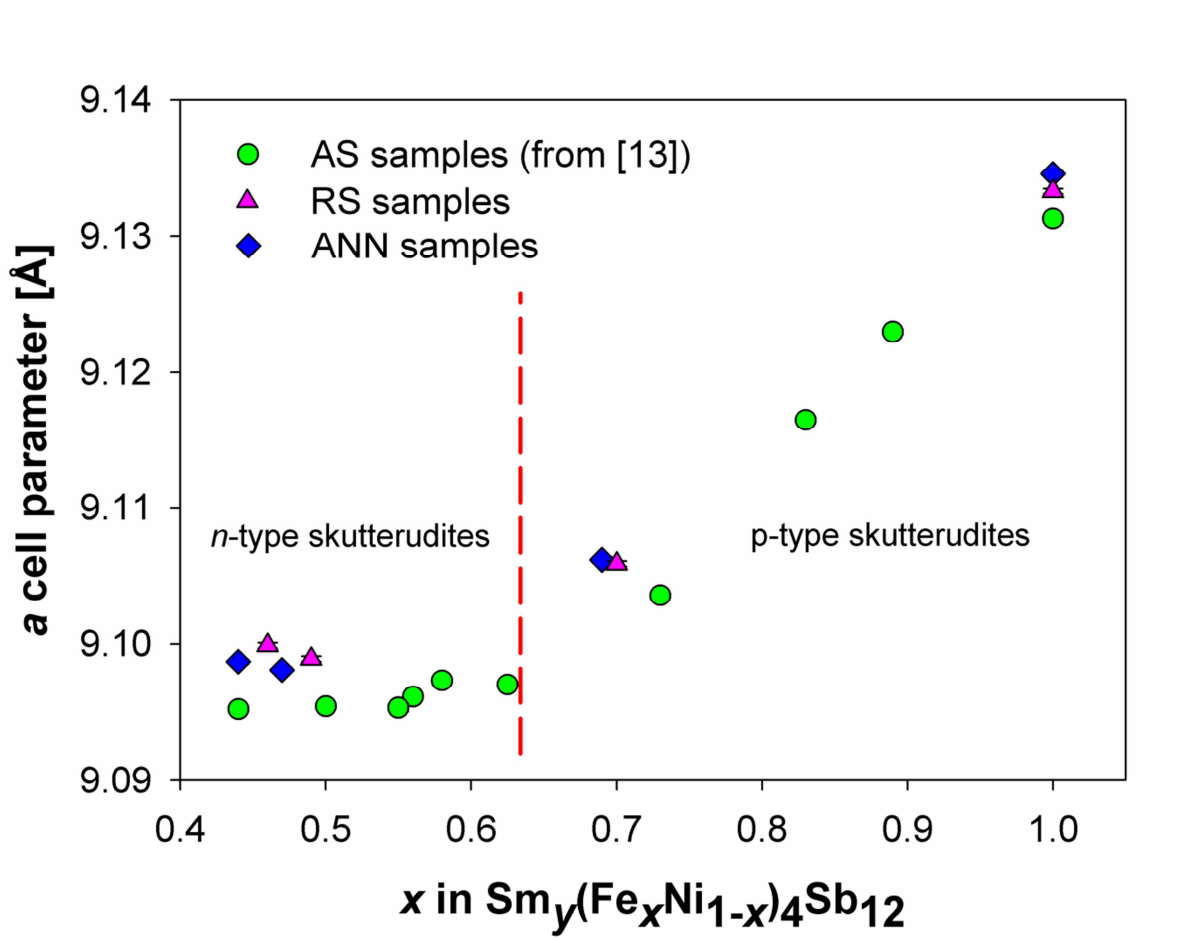
AS samples (from [13])
RS samples
ANN samples
n-type skutterudites
p-type skutterudites
a cell parameter [Å]
x in Sm_y(Fe_xNi_1-x)_4Sb_12
9.14
9.13
9.12
9.11
9.10
9.09
0.4
0.5
0.6
0.7
0.8
0.9
1.0

Figure 4

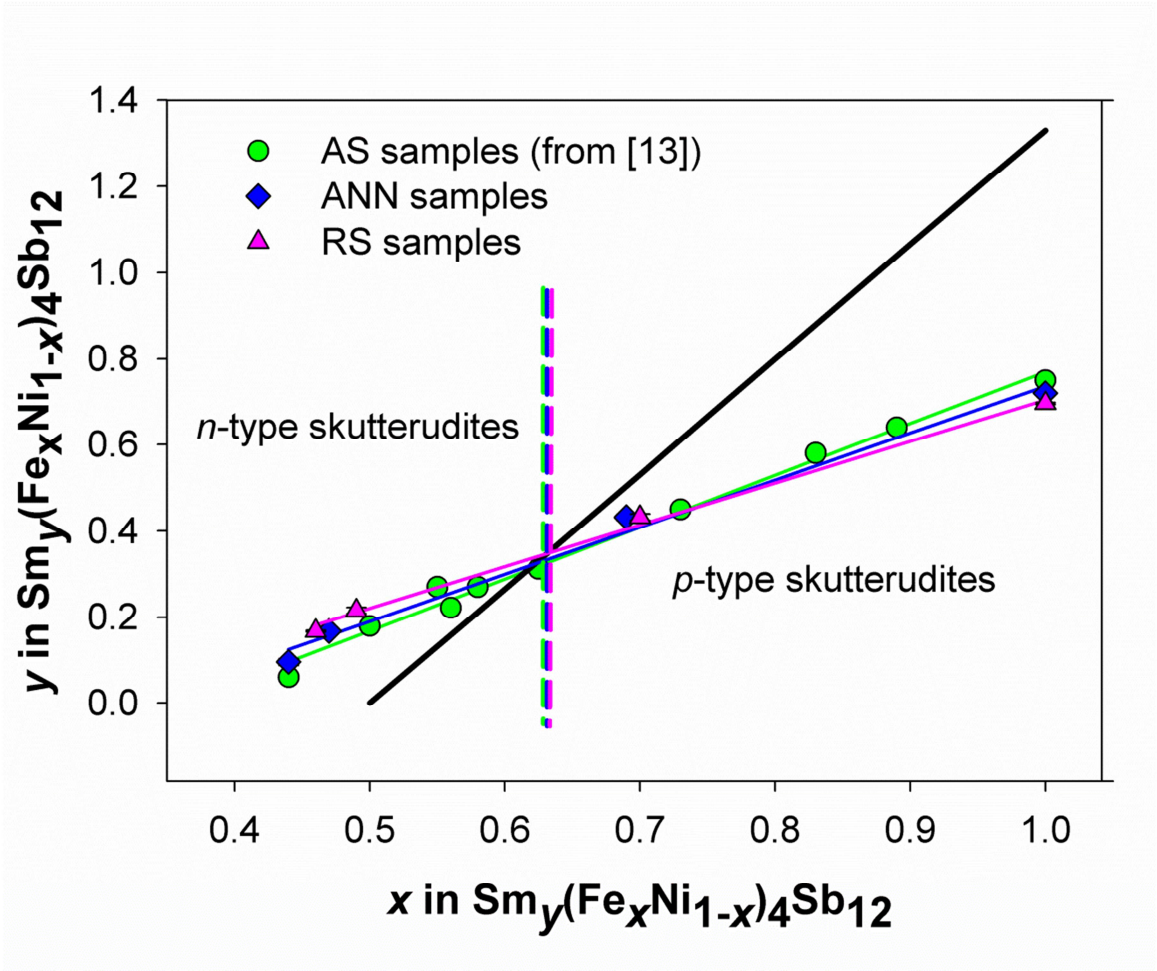
AS samples (from [13])
ANN samples
RS samples
n-type skutterudites
p-type skutterudites
y in Sm_y(Fe_xNi_1-x)_4Sb_12
x in Sm_y(Fe_xNi_1-x)_4Sb_12
1.4
1.2
1.0
0.8
0.6
0.4
0.2
0.0
0.4
0.5
0.6
0.7
0.8
0.9
1.0

Figure 5

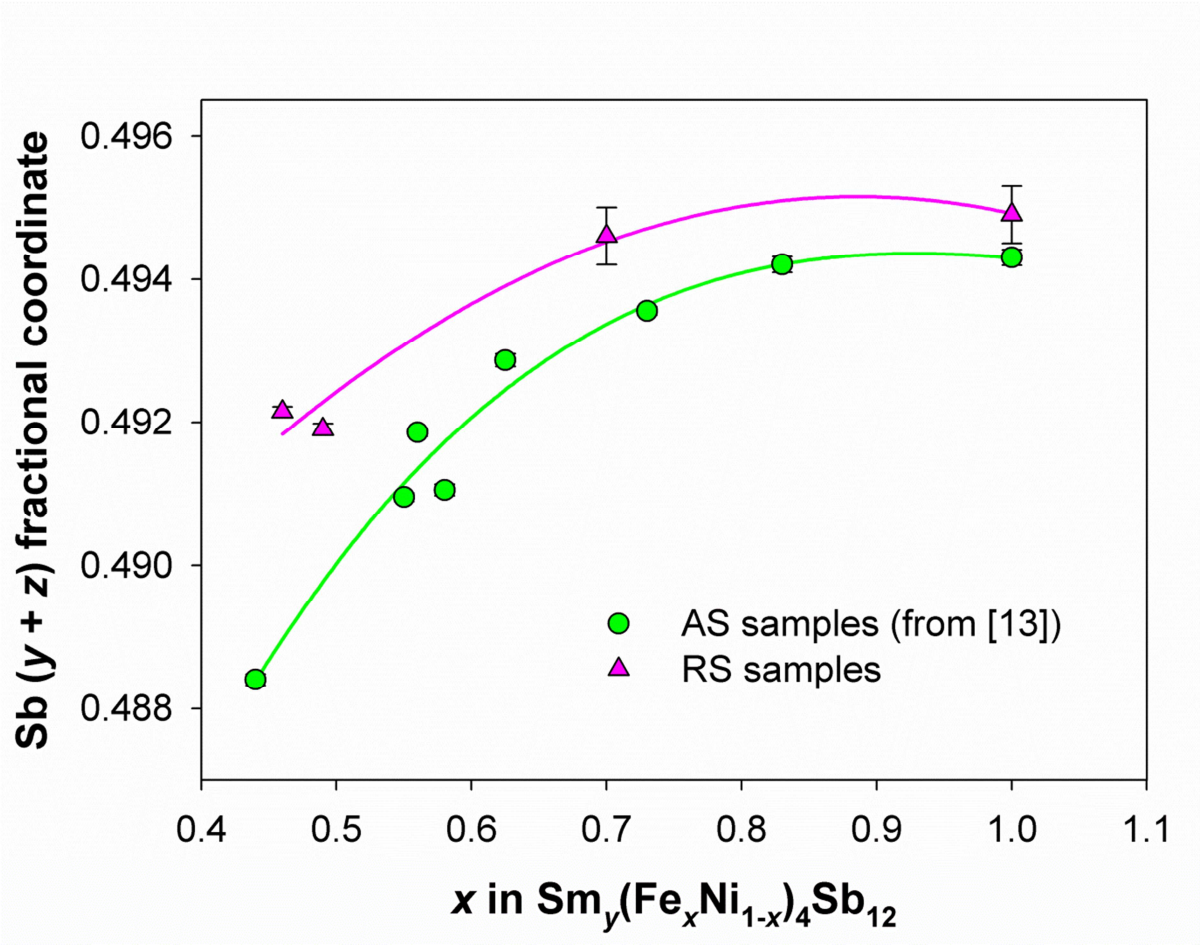
Sb (y + z) fractional coordinate
0.496
0.494
0.492
0.490
0.488
0.4
0.5
0.6
0.7
0.8
0.9
1.0
1.1
x in Sm_y(Fe_xNi_1-x)_4Sb_12
AS samples (from [13])
RS samples

Figure 6

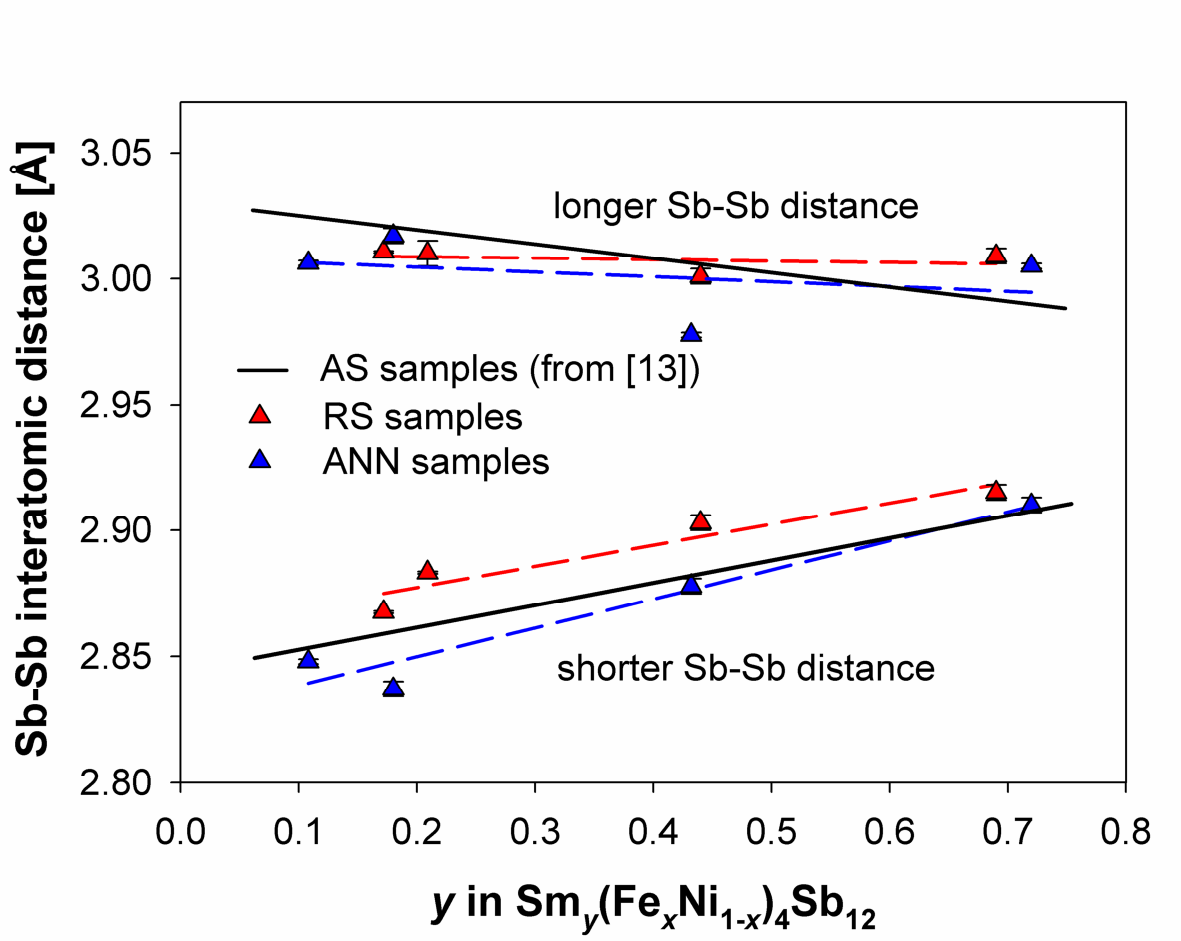
Sb-Sb interatomic distance [Å]
3.05
3.00
2.95
2.90
2.85
2.80
0.0
0.1
0.2
0.3
0.4
0.5
0.6
0.7
0.8
longer Sb-Sb distance
AS samples (from [13])
RS samples
ANN samples
shorter Sb-Sb distance
y in Sm_y(Fe_xNi_1-x)_4Sb_12

Figure 7

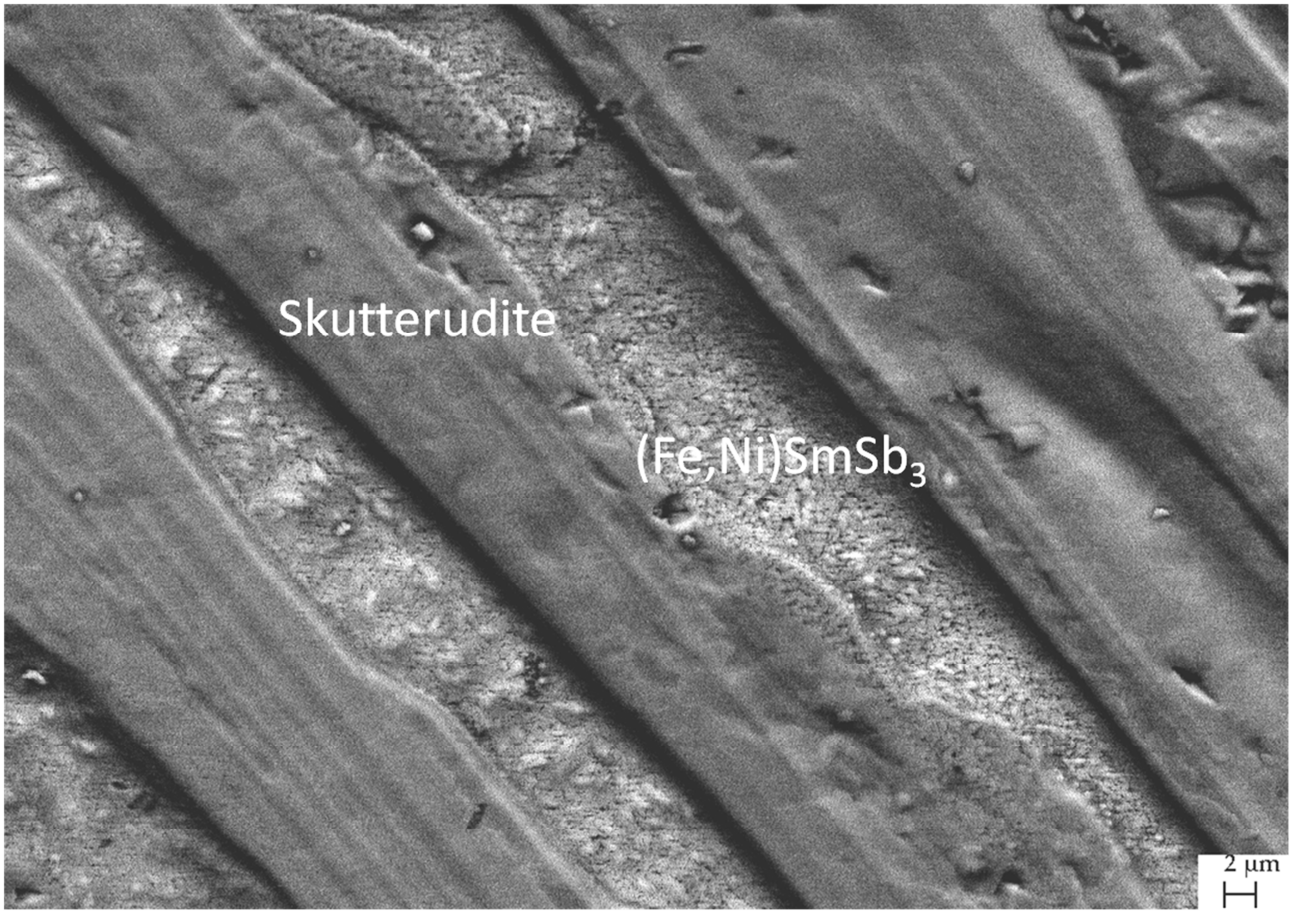

Figure 8

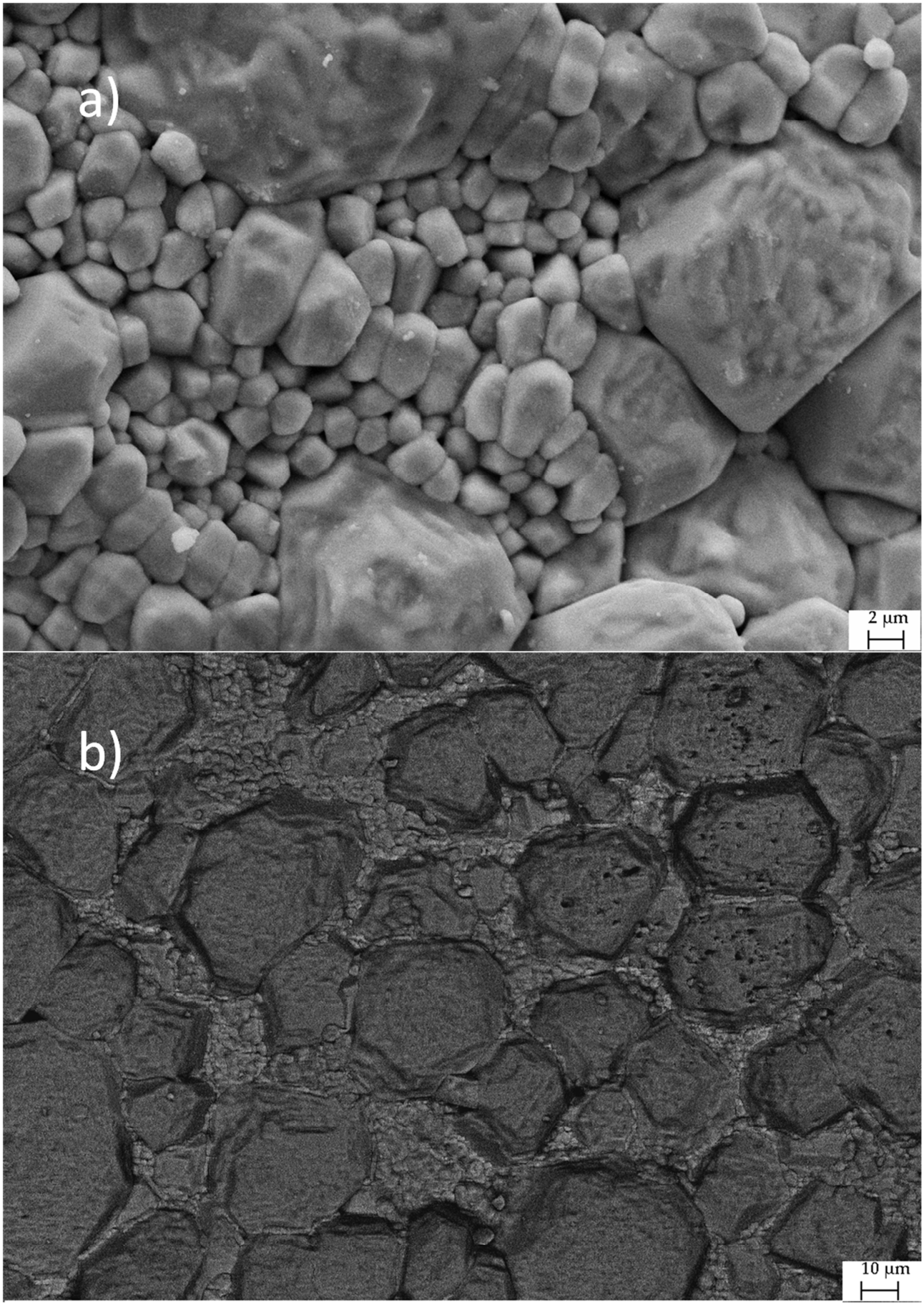

Figure 9

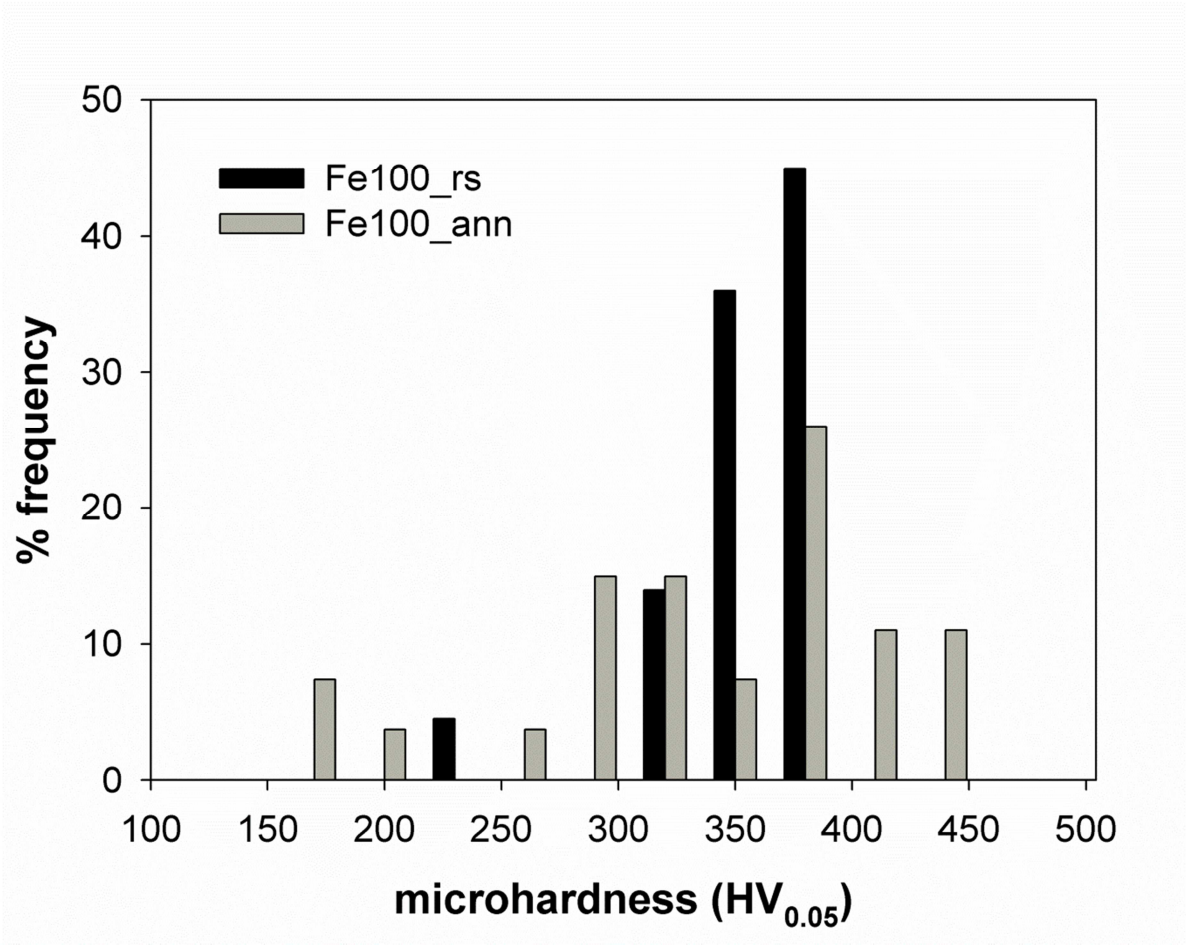
Fe100_rs
Fe100_ann
% frequency
0
10
20
30
40
50
100
150
200
250
300
350
400
450
500
microhardness (HV0.05)

Figure 10

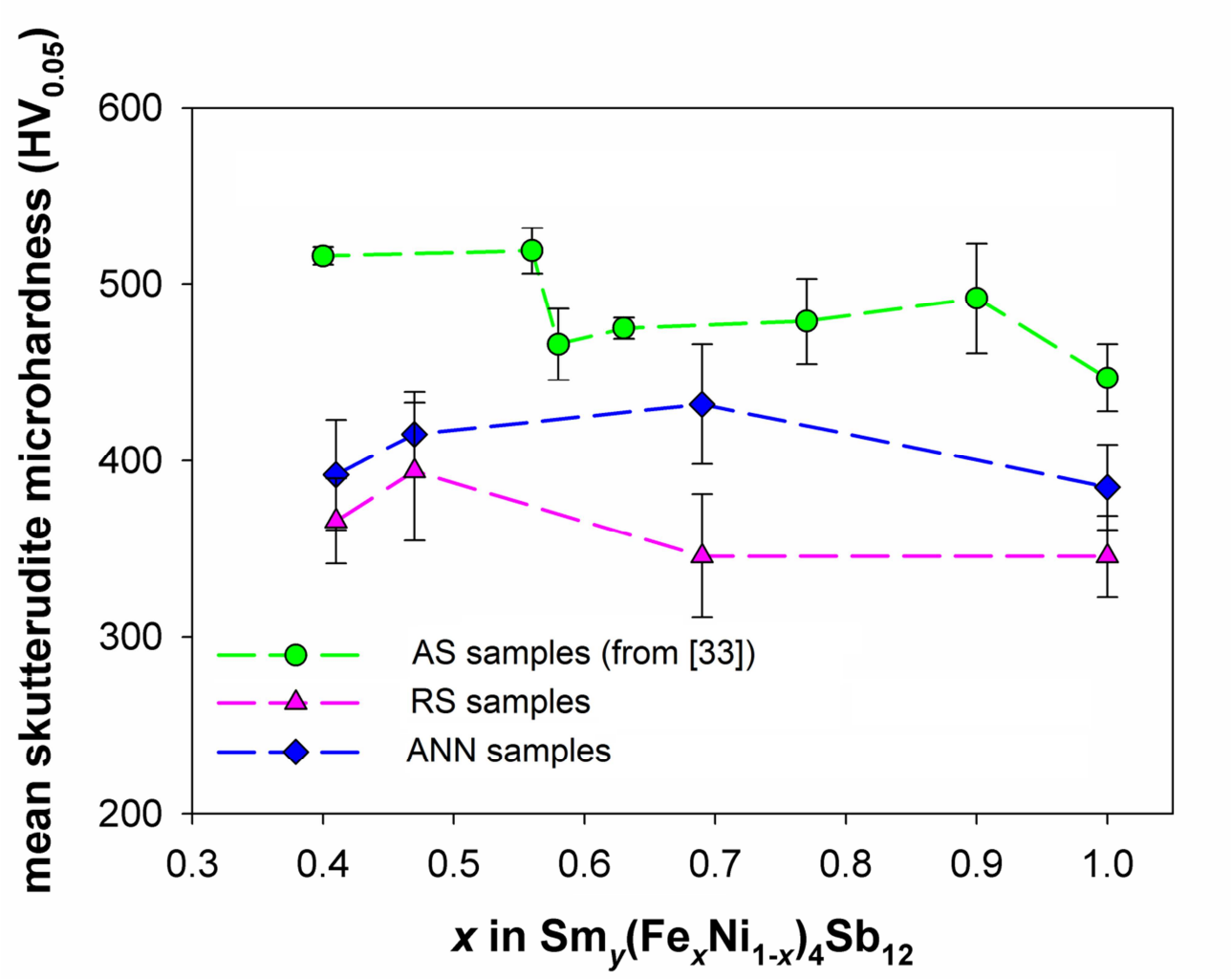
mean skutterudite microhardness ($HV_{0.05}$)
600
500
400
300
200
0.3
0.4
0.5
0.6
0.7
0.8
0.9
1.0
AS samples (from [33])
RS samples
ANN samples
x in $Sm_y(Fe_xNi_{1-x})_4Sb_{12}$